CHEMISTRY
A European Journal

Accepted Article

Title: Sonochemical Formation of Copper/Iron-modified Graphene Oxide Nanocomposites for Ketorolac Delivery

Authors: Darya Radziuk

This manuscript has been accepted after peer review and appears as an Accepted Article online prior to editing, proofing, and formal publication of the final Version of Record (VoR). This work is currently citable by using the Digital Object Identifier (DOI) given below. The VoR will be published online in Early View as soon as possible and may be different to this Accepted Article as a result of editing. Readers should obtain the VoR from the journal website shown below when it is published to ensure accuracy of information. The authors are responsible for the content of this Accepted Article.

To be cited as: *Chem. Eur. J.* 10.1002/chem.201900662

Link to VoR: http://dx.doi.org/10.1002/chem.201900662

WILEY-VCH

Sonochemical Formation of Copper/Iron-modified Graphene Oxide Nanocomposites for Ketorolac Delivery

Darya Radziuk,*[a] Lubov Mikhnavets,[a] Mykhailo Vorokhta,[b] Vladimír Matolín,[b] Ludmila Tabulina[a], and Vladimir Labunov[a]

Abstract: A feasible sonochemical approach is described for the preparation of copper/iron-modified graphene oxide nanocomposites by using ultrasound (20 kHz, 18 W/cm^2) in aqueous solution containing copper and iron ion precursors. Unique copper-, copper/iron- and iron-modified graphene oxide nanocomposites have a submicron size that is smaller than pristine GO and a higher surface area enriched with Cu_2O, CuO, Fe_2O_3 of multiform phases (α-, β-, ε- or γ), FeO(OH) and sulfur- or carbon-containing compounds. These nanocomposites are sonochemically intercalated with the nonsteroidal anti-inflammatory drug ketorolac resulting in formation of nanoscale carriers. Ketorolac monotonically disintegrates from these nanoscale carriers in aqueous solution adjusted to pH from 1 to 8. The disintegration of ketorolac proceeds at a slower rate from the copper/iron-modified graphene oxide at increased pH, but at a faster rate from the iron-modified graphene oxide starting from acidic conditions.

Introduction

Nonsteroidal anti-inflammatory drugs (NSAIDs) are among the most commonly prescribed medications worldwide to treat the inflammation and pain, thereby reducing fever and inhibiting the thrombocyte aggregation.[1] Among many NSAIDs ketorolac is related to the type of pyrroles being most potent and effective analgesic to be used after surgery with efficacy comparable to opioids.[2] Ketorolac's pyrrolizidine carboxylic acid derivative is structurally related to indomethacin acting as cyclooxygenase-2 (COX-2) inhibitor. Recently ketorolac demonstrated down regulation of the expression of regulatory subunit of Casein Kinase 1 in Wnt–β-Catenin Signaling, *i.e.* DDX3, being involved in the progression of several types of cancer.[3] The anticancer activity of ketorolac can be associated with its free binding energy being closer to DDX3 inhibitors, its capability to form strong hydrogen bonds similar to crystallized DDX3 protein and to inhibit the ATP hydrolysis decreasing the number of neoplastic lesions. Ketorolac also suppresses early breast cancer relapse and improves its postoperative oncological outcome.[4] Ketorolac's anticancer effects and its aptitude to deactivate inflammatory pathways can be particularly useful in retardation of tumor growth.[5]

Commonly ketorolac is administered as the tromethamine salt orally, intramuscularly, intravenously, or as a topical ophthalmic solution. It is considered a first-generation NSAID with the efficacy being 800 times higher than aspirin and biological half-life of 4-6 h.[6] Ketorolac is non-addictive in nature and does not induce nausea and respiratory side effects. However, in its most frequent form, *i.e.* the oral tablet, the drug is delivered to the human body through the gastro-intestinal system, which undergoes bleeding and develops gastritis after repeated doses over prolonged administration.[7] In addition, its ability to selectively inhibit COX2 has important cardiovascular side-effects that include increased risk for myocardial infarction, stroke, heart failure and hypertension.[8] For human health benefits one has to consider appropriate approaches for the administration of ketorolac at a lower dose over shorter period of the systemic exposure while maintaining its therapeutic efficacy.[9]

Nanomedicine offers beneficial approaches based on objects at the nanoscale aiming at an increase of the drug surface area by reducing its size and modifying its surface to facilitate more rapid dissolution and absorption by a target tissue.[10-17] Moreover, it provides techniques for safe handling and methods for minimizing toxicity of nanoscale carriers for the *in vivo* application.[18-21] These nanoscale carriers can significantly improve the bioavailability of drug and decrease the dose of administration, thereby enhancing its therapeutic efficacy with lower side effects. The anti-inflammatory activity of NSAIDs can be enhanced through the formation of Cu(II)-complexes with drugs functionalized with the carboxylate group operating as a bridging ligand involving Cu-O and Cu-Cu bonds in the complexes undertaking the enzyme superoxide dismutase (SOD).[18] In addition, the CuO derivatives have a high oxygen radical scavenger activity and the peripheral parts of the complex molecules are mostly hydrophobic in character.[22] These neutral binuclear molecules with a high peripheral hydrophobicity can exert a SOD-like activity once the apical positions on Cu(II) are made free, which can be useful in the understanding of the drug-metal and drug-enzyme interactions. Importantly, the copper carboxylates drugs constitute an important element of anti-inflammatory and anticancer agents, some of which are a part of several commercially available drugs.[23]

The complexation of NSAIDs with other metals such as Cd (II), Pt (II), Fe (II), Ni (II) or Zn (II)[24,25] leads to the scavenging of free radicals (incl. oxygen) and results in enhanced gastric protection.[26] This improved pharmacological

[a]   Dr. Darya Radziuk,* Lubov Mikhnavets, Dr. Ludmila Tabulina and Prof. Vladimir Labunov
        Laboratory of Integrated Micro- and Nanosystems,
        Belarusian State University of Informatics and Radioelectronics,
        P. Brovki Str. 6, 220013 Minsk, Republic of Belarus
        E-mail: dasharaduk@gmail.com
[b]   Dr. Mykhailo Vorokhta and Prof. Vladimír Matolín
        Department of Surface and Plasma Science,
        Charles University of Prague,
        V Holešovičkách 2, 18000 Prague 8, Czech Republic

        Supporting information for this article is given via a link at the end of the document.

activity of metal complexes of active drugs as ligands can derive from the synergistic effects of the ligand and the coordination residue upon the decomposition of the molecular metal-NSAID complex or an intrinsic high activity of the complex itself, the neutralization of overall negative charges on the drug molecule upon the complex formation, superior transport process through the cell membranes due to the changes of the hydrophobicity/hydrophilicity ratio. The anti-inflammatory, anti-pyretic and analgesic activity of drug can be improved through the formation of the Fe(III)-peptide complex yielding the ligand moieties containing oxamide functionality.[27] Other studies show the antibacterial efficiency of some Fe(III)-NSAID complexes: i) the Fe(III)-paracetamol complexes can enhance the inhibitory effect against E. coli[28] and ii) the Fe(III)-lornoxicam (LOR) complex can inhibit the bacterial growth capacity for the Staphylococcus aureus due to the ability of the complex to cross a cell membrane and inactivate the pathogens secreting various enzymes, which are involved in the breakdown of activities.[29] Importantly, the Fe(III)-complex can facilitate the ion diffusion through the lipid layer of the spore membrane to the site of action and ultimately kill them by combining with the OH, SO_2 and C=N groups of certain cell enzymes. On the other hand, the metal complex of Fe(II) can be very active against breast cancer cell line (MCF7) with inhibition ratio values between 74-86 %.

Other approaches in minimizing dosage can be based on NSAID encapsulation, which utilize a nanoscale carrier that transports the active drug ingredient and facilitates controlled release at the therapeutic target site.[30-32] This strategy can overcome issues with the drug solubility, prevent degradation in the gastrointestinal system, improve the bioavailability at the therapeutic site, and reduce the systemic exposure. Still a major obstacle of the encapsulation approach is the uptake of nanoscale carriers by macrophages and subsequent clearance of the drug.[33,34]

Graphene oxide (GO) can be used as a nanoscale carrier for a drug due to its high surface area, biocompatibility and a very rich surface chemistry offering a wide choice for the smart design of effective drug delivery platform.[35-39] GO can remain for a long time in a body and have good biocompatibility, but size, shape, agglomeration state and toxicity (presence of contaminants) can cause undesired inflammation.[33,40] GO biodegradation can be modulated by dispersion and digestion by peroxidases naturally present in cells. Appropriate GO purification and modification can increase the efficacy of drug loading in GO and optimize adsorption/desorption kinetics at minimal toxicity.[41-44] The rich GO surface chemistry facilitates functionalization with diverse molecular compounds: dyes,[45] inorganic[45-48] and organic (DNA,[49] ssRNA,[50] gene[51]) substances, polymers,[52-55] luminescent or fluorescent particles[56,57] enabling synergistic effect of drug delivery and bioimaging[58-61] of a carrier platform. Immobilization with drug molecules can regulate the GO dispersal in water or in the cell culture media, reduce its cell/tissue toxicity and induce accumulation to the target cells and tissues.[62-65] Drug release from GO can be activated by the pH gradient naturally present in the cells/tissues through the distortion of the interactions between the drug and GO nanocomposite.[53]

Sonochemistry is an efficient tool to construct multifarious molecular carriers for resourceful drug delivery,[66] and it derives from acoustic cavitation, which is the formation, growth and implosive collapse of gaseous bubbles, acting as highly energetic hot spots.[67] These hot spots can reach 5000 K and

10^3 bar in a bulk aqueous solution producing sonolysis of water.[68] Sonolysis of water generates OH· and H· radicals and the primary products such as H_2, H_2O_2 and $HO_2^.$ performing redox reactions.[69] Sonochemistry is being actively involved in the molecular assembly and encapsulation processes through the cross-linking mechanisms (disulfide bond formation) in proteins[70] that retain their biological function. In many cases superoxide ($HO_2^.$) is the principal cross-linking agent.[69,71] To date, this sonochemical pathway has been very successful in the encapsulation of antibiotic nanoparticles in GO[62] that is immaculate or modified with Ag,[72] Fe_3O_4,[73] Au[74] and their bimetallic compounds.[75] Nowadays little is known about the sonochemical formation mechanism of hybrid copper/iron GO nanocomposites and much less about the NSAID intercalation into their structure.

For the first time, we introduce a convenient sonochemical method for the preparation of a hybrid copper/iron-modified GO nanocomposite and reveal its formation mechanism. The complexation of the ketorolac with copper, copper/iron or iron can be useful in the understanding of the drug-metal or drug-metal oxide interaction for the fundamental studies of the drug-enzyme reactions, of the crossing the cell membrane and activation of the breakdown activities. Here we also report on the sonochemical intercalation of ketorolac into this unique material and disclose its degradation in aqueous solution being adjusted to a pH from 1 to 8. The pH values were chosen for the reason of comparison with the cellular media of human gastric juice in stomach (~ 1.5-3.7),[76] lysosomes (~ 4.3-5.3),[77] urine (~ 5.9-6.7),[78] duodenum (~ 6.0-8.0),[79] and pancreas or insulin secretion (~ 5.0-10.5).[80]

Results and Discussion

The successful GO formation (sample N1) was confirmed through the characterization of its physico-chemical properties by using X-ray powder diffraction, Raman microscopy and thermogravimetric analysis (**Figure S1**, see more details in the supporting information). These synthesized GO were sonochemically modified with copper and iron compounds at the first step and the sonochemical intercalation of the anti-inflammatory drug ketorolac into their structure at the second step (**Scheme 1**).
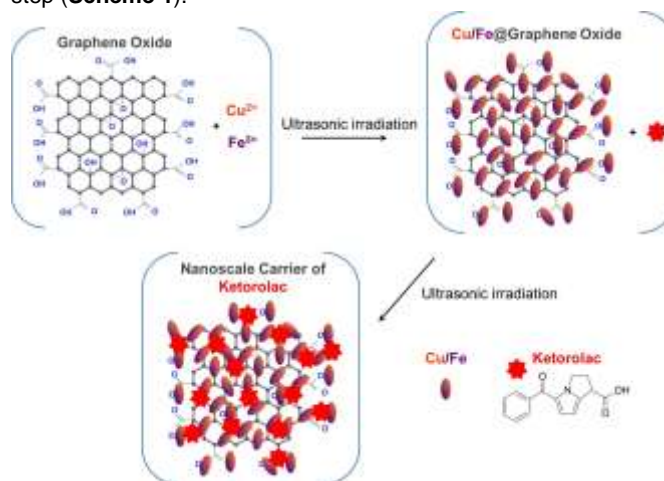
Scheme 1. Schematic illustration of the sonochemical modification of synthesized graphene oxide (GO) in aqueous solution containing copper and

iron compounds at the first step, and subsequent ultrasonic intercalation (20 kHz, 18 W/cm², 3 min, horn-type ultrasonic disperser) of the copper/iron-modified@GO nanocomposite by ketorolac (NSAID drug) in aqueous solution.

Ultrasound with a horn type (20 kHz, 18 W/cm²) was used to prepare copper- (sample N2), copper/iron- (sample N7) and iron@GO nanocomposites (sample N9) in aqueous solutions containing Cu^{2+} and Fe^{3+} ion precursors. **Figure 1A** demonstrates synthesized GO before the sonochemical surface modification, showing nanomaterial with a size distribution ~ 500 nm (relative standard deviation, r.s.d. ≈ 25%) (Figure S1A).
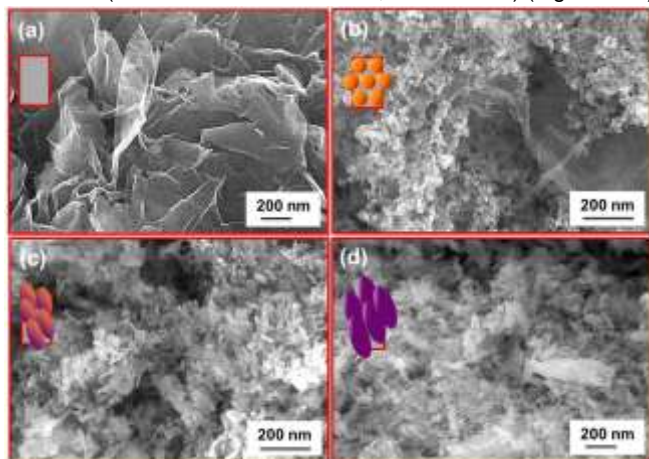

Figure 1. Representative SEM images of (a) synthesized graphene oxide (GO) and sonochemically prepared nanocomposites: (b) copper@GO (sample N2), (c) copper/iron@GO (sample N7) and (d) iron@GO (sample N9).

SEM image of N2 nanocomposite reveals GO with a decorated spherical morphology (**Figure 1B**), which changes into elongated nanostructure in the shape of a grain rice of smaller size in sample N7 (~ 580 nm, r.s.d. ≈ 16%) (**Figure 1C**) and of larger size in sample N9 (~ 460 nm, r.s.d. ≈ 3%) (**Figure 1D**). These sonochemically formed morphologies are clearly distinct from nanoparticles that were ultrasonically grown on the external walls of sonicated multi-walled carbon nanotubes functionalized with the carboxylic acid groups, *i.e.* f_{CA}-MWCNTs, from our previous studies.[81] In contrast to graphene oxide nanocomposites, those erbium carbioxoxide nanoparticles appeared with the nonuniform geometry and a broad diameter distribution from 50 to 200 nm, the size being comparable to the highly fluorescent polymeric nanoparticles that exhibit the 4.5-fold increase in the quantum efficiency, when compared with the free dye molecules in water.[82] Importantly, the presence of GO leads to the growth of nanoparticles with a more pronounced morphology that has a spherical or elongated rice-like shape than carbon nanotubes being used as a template material. On the other hand, ultrasonic treatment with the carbon nanotubes yields smaller nanoparticles than those with GO. We assume that GO provides a larger surface area enriched with higher amount of oxygen containing chemical groups than carbon nanotubes resulting in the enhanced nanoparticle's growth with a more defined morphology.

Volume composition of copper/iron-modified@GO nanocomposites

In **Figure 2** the phase composition of synthesized GO before and after sonochemical surface modification with copper and iron compounds was revealed by the X-ray powder diffraction analysis in accordance with the XRD database (**Table S1**).
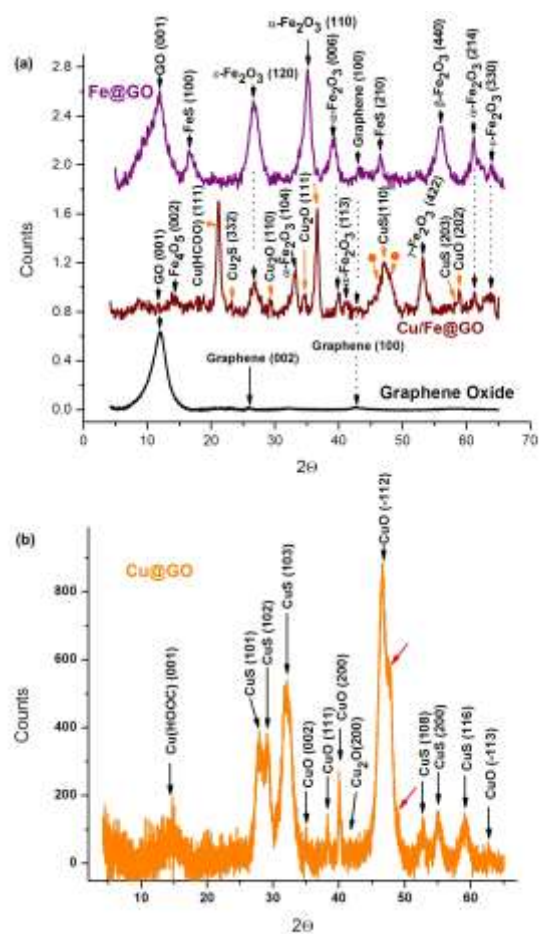

Figure 2. X-Ray powder diffraction patterns of (a) synthesized GO (sample N1, black line) and sonochemically prepared nanocomposites: copper/iron@GO (sample N7, wine line), iron@GO (sample N9, violet line) and (b) copper@GO (sample N2, orange line). (a) Circles of orange color indicate Cu_2S (046) at 2θ=46.5 and (12 4 2) at 47.9. (b) The crystalline phases in N2 nanocomposite are indicated by black arrows as following (001) at 2θ=14.5 of Cu(HOOC); (101) at 27.6, (102) at 29.2, (103) at 31.9 of CuS; (002) at 34.9, (111) at 38.4, (200) at 40.0 of CuO, (200) of Cu_2O (at 42.1), (108) at 52.8(200) at 55.1 and (116) at 59.0 of CuS; and (-113) at 62.7 of CuO according to the databases in the Table S1. Red arrows indicate strong peak at 2θ=46.4 being assigned to the (-112) plane of CuO considering its shift from 2θ=48.8.

XRD pattern shows the GO phase due to the presence of a characteristic peak at 2θ=11.9 arising from (001) plane, more details in supporting information (**Figure S1B**). The phase composition of N7 nanocomposite is dwelled in the successful formation of cuprite Cu_2O with characteristic reflections (110) and (111); tenorite CuO with the plane (202); hematite α-Fe_2O_3 with (104), (110), (006), (113) and (214) planes; maghemite γ-Fe_2O_3 with (422) plane; ε-Fe_2O_3 with (120) plane; recently discovered Fe_4O_5[83] with (002) plane; covellite CuS with (203) and (110) planes; Cu_2S with (332), (046) and (12 4 2) planes, and GO with (001) plane (**Figure 2A**). In this nanocomposite the XRD (001) plane of GO is very weak, indicating large range atomic coherence. The relatively larger d-spacing of GO may also indicate the formation of oxygen-containing functional groups in metal oxides in the sonochemically modified GO.[84] Most prominent peaks arise from (111) Cu(HCOO), (111) Cu_2O, (110) CuS, (104) α-Fe_2O_3 and (422) γ-Fe_2O_3, indicating that N7

FULL PAPER Accepted Article

nanocomposite indeed contains copper and iron oxides as well as copper sulfide.

The elemental composition of N7 nanocomposite was obtained from the EDX spectra (**Table 1**). N7 nanocomposite is composed of C (35.6 atom.%), O (44.5 atom.%), Cu (1.7 atom.%), Fe (13.8 atom.%) and S (2.6 atom.%), in agreement with the XRD analysis (**Figure 2A**). In contrast, N1 contains only higher amount of C (58.7 atom.%), but lower concentration of O (39.5 atom.%). The amount of sulfur in N1 is twice less than in N7 nanocomposite. We attribute these changes in the elemental composition to the ultrasonic effects on the GO nanostructure (*e.g.* defect formation and intercalation of S in the carbon lattice)[85] and to the sonochemical redox reactions between copper, iron, sulfur (acting as reductant) and radical species, *i.e.* hydrogen (reductant); hydrogen peroxide, hydroxyl and oxygen acting as oxidants.[69]

The dominant (111) XRD peak of Cu_2O is relatively sharp, demonstrating the presence of a material larger than 5 nm in N7 (**Figure 2**). Very small (110) peak of Cu_2O may result from nanocrystal partial reduction post synthesis involving diffusion of atoms and lattice expansion process, which may be limited to atom rearrangement and lattice/unit cell reconstruction yielding rich Cu_2O phase (*i.e.* copper in oxidized state). We assume that complete transformation of Cu_2O to crystalline CuO does not occur because of the following possible reasons: i) sonochemical reactions involving reductants such as Na_2S and radicals (*i.e.* $H_2^·$) and oxidants (*i.e.* $OH^·$, $H_2O_2^·$, $HO_2^·$); ii) there is a considerable energetic difference between the *Pn3* group of Cu_2O and monoclinic *C2/c* group of CuO structure; iii) Cu_2O has the high-symmetry cubic and CuO has a low-symmetry monoclinic structure; iv) there may be possible stabilization of the (I) oxidation state by the carbon network of GO and the present Fe^{3+} ions. This carbon network of GO can be ultrasonically doped by S^{2-} due the presence of Na_2S resulting in the formation of reduced S-GO nanostructure, and later CuS synthesis through the sonochemical reduction of Cu(II).[86] Indeed, XRD reveals CuS, Cu_2O and CuO phases in N2 nanocomposite, indicating that Cu(I) phase may be stabilized by the carbon lattice network of GO containing intercalated sulfur as a result of interaction with the sonochemically produced radicals, Cu^{2+} and S^{2-} ions (**Figure 2B**).

Three crystal structures of Fe_2O_3: γ-ε-α as well as rare Fe_4O_5 phase were revealed in N7 nanocomposite, showing that the phase transformation may take place depending on the particle size, temperature or pressure during the sonochemical synthesis.[86-88] Most of these XRD peaks are relatively small, but not significantly broadened, denoting the formation of nanoparticles smaller than submicron size, in agreement with the SEM in Figure 1B. The XRD pattern reveals α-Fe_2O_3 (≈ 80%) as the main phase along with γ-Fe_2O_3 (≈ 10%), ε-Fe_2O_3 (≈ 7%) and Fe_4O_5 (≈ 3%). In this iron oxide polymorph structure the most thermodynamically stable form is α-Fe_2O_3. Other metastable polymorphs can be stabilized during the decrease of the iron oxide crystallite size.[88] Another parameter is the reaction temperature: at 530°C all these polymorphs can be formed, while heating to 650°C may lead to the disappearance of γ-Fe_2O_3 and ε-Fe_2O_3 phases, and leaving α-Fe_2O_3 at 700°C. Such high temperatures can arise during the acoustic cavitation, which forms highly energetic hot spots upon the bubble collapse (T ≈ 5000 K and P ≈ 10^3 atm) in the bulk solution.[68] The existence of these conditions is confirmed by the presence of a high-pressure and high-temperature polymorph of iron oxide

Fe_4O_5, which is stable from 5 to at least 30 GPa.[83] Fe_4O_5 can be readily synthesized at 10 and 20 GPa, upon heating at 1500-2200 K. This recently discovered phase can result from the breakdown of magnetite into Fe_4O_5 and Fe_2O_3. The magnetite can be also formed as a result of transformation of γ-Fe_2O_3 under 600 K[89] and due to the sonochemical reduction of Fe^{3+}.[90] There is no β-Fe_2O_3 in our nanocomposites, which can be a result of longer thermal treatment during sonication, indicating the existence of independent transition chain γ-Fe_2O_3 → ε-Fe_2O_3 → α-Fe_2O_3. Other factors such as increase of the α-Fe_2O_3 particle size may contribute to the formation of the *β* polymorph.[91]

Table 1. Elemental composition of synthesized GO (sample N1) and sonochemically prepared copper@GO (sample N2), copper/iron@GO (sample N7) and iron@GO (sample N9) obtained from the EDX spectra.

Sample	C atom.%	O atom.%	Cu atom.%	Fe atom.%	S atom.%	Na atom.%
N1	58.7	39.5	-	-	1.3	-
N2	33.4	18.2	28.1	-	17.8	-
N7	35.6	44.5	1.7	13.8	2.6	-
N9	58.5	29.9	0.1	5.6	2.3	1.2

XRD discloses (001) plane of GO and the following phases (110), (006) and (214) α-Fe_2O_3; (120) and (330) ε-Fe_2O_3; (440) β-Fe_2O_3, (100) and (210) FeS along with (100) graphene in N9 nanocomposite (**Figure 2A** and **Table S1**). In contrast to N7, in XRD pattern of N9 the (100) plane of GO disappears and (001) plane of GO appears as intense and broad reflection, indicating the layered structure of nanocomposite with a very short range atomic coherence. Strong XRD (001) peak is characteristic of GO because it shows oxygen containing functional groups on carbon sheets. To note, the γ-Fe_2O_3 phase was not revealed in XRD pattern. The presence of polymorph metastable ε-Fe_2O_3 and β-Fe_2O_3 phases, which exhibit relative intensity comparable to that of the α-Fe_2O_3 phase may result from high heating/cooling rates (*i.e.* > 10^7 K/s) during acoustic cavitation, which can lead to the partial or complete amorphization or recrystallization of material.[92] The layered structure of GO doped by Fe^{3+} ions may act as a buffer against transition to the α-Fe_2O_3 phase in aqueous solution. The existence of the transition chain ε-Fe_2O_3 → α-Fe_2O_3 without γ-Fe_2O_3 shows effects of high temperature during the sonochemical synthesis. Typically ε-Fe_2O_3 is an intermediate polymorph between γ-Fe_2O_3 and α-Fe_2O_3. The formation of the γ-Fe_2O_3 phase requires the presence of Fe_3O_4 at 300°C, but XRD does not reveal this phase in material[93] because of the absence of Fe_4O_5.[83] On the other hand, there is a FeS phase, which is a very stable crystalline phase even at 800°C and under pressure of up to several GPa. We assume that FeS may be formed according to the mechanism similar to copper sulfide, in agreement with our recent work.[55] In this way, the difference in the composition between copper- and iron-modified@GO nanocomposites may be attributed to the characteristic electrochemical potential of Cu (0.153 J/mol) and Fe (-0.037 J/mol), implying that more energy may be required for the reduction of Fe^{3+}.

Surface chemical composition of copper/iron-modified@GO nanocomposites

Figure 3 parts A and B show the surface chemical composition and bonding of synthesized GO (N1) and sonochemically prepared nanocomposites (N2, N7 and N9). In **Figure 3A** N1 is mainly composed of C and oxygen containing surface groups (C/O = 1.7 atomic ratio, **Table 2**) and a small

amount of S (0.6 atom.%). The surface groups are the following: carbonyl (R-C=O-R'), epoxide (R-C-O-C-R') and carboxyl (C(=O)OH).[94]

We assume that the carbon lattice is not intercalated by S (high C/S ratio ~ 105) and sulfur undergoes oxidation during ultrasonic dispersion of GO in the aqueous solution. Sulfur has several oxidation states and tends to stabilize into SO_4 (O/S ~ 62). The lower energy C1s line at ~ 284.5 eV (C-C bond in all samples) is assumed to be rather generic aliphatic than graphitic carbon (~ 284.0 eV).[95] Another C1s component at ~ 286.7 eV (in all samples) is attributed to the π-π* shake-up bands of the highly aromatic 18π electron system and can be assigned to the C-O bond. The OH group may also present in the GO structure because its C 1s binding energy is similar to the epoxide group (C-O-C).[96] The lower energy C1s line is indicative for the sp^2-hybridized graphite consisting of the hexagonal network of parallel carbon layers with covalent bonding between C-C atoms within a plane. The higher energy C1s component is attributed to the sp^3-hybridized carbon atoms with a typical diamond structure. Overall, the ratio of all samples is higher with the sp^3 hybridized carbon chemical state that is related to a diamond structure with a C-C bond length ~ 0.15 nm.
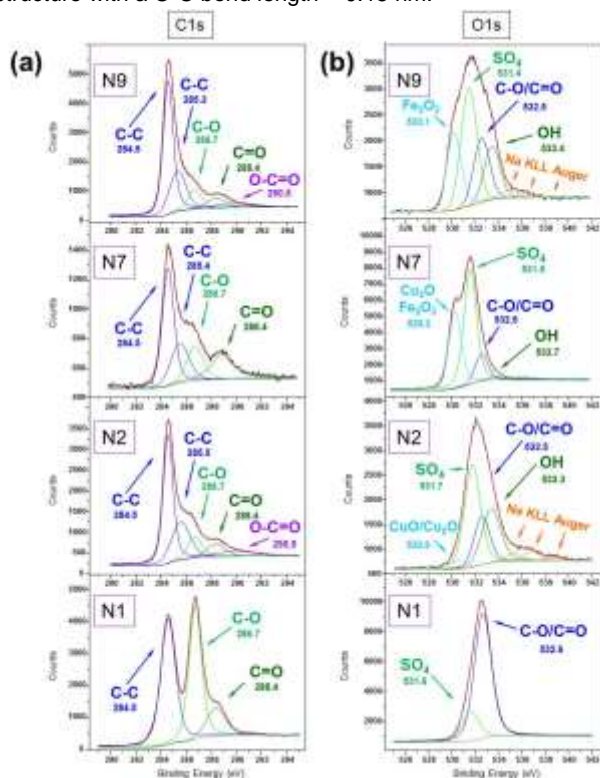

Figure 3. Representative XPS spectra of synthesized GO (sample N1), copper@GO (sample N2), copper/iron@GO (sample N7), and iron@GO (sample N9) nanocomposites: (A) XPS C 1s and (B) O 1s. The curve fitting of the C1s (A) and O1s (B) spectrum was performed using a Gaussian-Lorentzian peak shape after performing a Shirley background correction. The color coding represents raw spectra (black) and their fits (red), and fitted peak components are presented in other colors.

To note, the sp^2-hybridization is related to the graphite, which consists of parallel carbon layers. The C1s component at ~ 288.4 eV (present in all samples) is indicative for the oxidized surface containing higher amount of oxygen.

From the C/O atomic ratio we assume that N7 is composed of excess of oxygen and oxygen-containing compounds (C/O ~

0.3) involving both copper and iron, and a much lower amount of carbon (**Table 2**). In N9 and N2 the amount of carbon is twice higher than oxygen (C/O ~ 2.4 and 2.1), but the surface enrichment with copper or iron oxides is comparable (O/Cu ~ 8 and O/Fe ~ 6). The increasing loss of oxygen could be associated with the oxygen-deficient regions (*i.e.* vacancies)[97,98] and the S ion doping effect. In contrast to N1, the binding energy of the C-C band in each type of nanocomposite shows another component at higher values ~ 285 eV (aromatic carbon), indicating that the separation between C and other atoms decreases. The binding energy of this second C-C component is systematically shifted by ~ 0.1 eV to the lower values being at ~ 285.5 eV (in N2), ~ 285.4 eV (in N7) and ~ 285.3 eV (in N9). In general the peak at 285 eV corresponds to the C-O or C-S suggesting that S ion can be intercalated into the carbon lattice.[85] To note, in N2 and N9 a small broad C1s component peak at ~ 290.5 eV discloses copper or iron carbonaceous compounds or their sulfides bound to the carbonyl groups of GO.[99] We will prove later in the text that this peak cannot be assigned to the presence of $CuCO_3$, $FeCO_3$ or iron-hydroxyl carbonate $Fe(OH)_2CO_3$.

In **Figure 3B** the XPS O1s line is introduced by two components in N1: main peak at ~ 532.6 eV (C-O/C=O) and minor peak at ~ 531.6 eV (SO_4). In N7 the O1s line is composed of four components being assigned to Fe_2O_3 and Cu_2O (530.2 eV), SO_4 (531.5 eV), C-O/C=O (532.5 eV) and OH (533.7 eV). We assume that the surface of N7 is more enriched with oxygen (C/O ~ 0.3) and sulfur (C/S ~ 5) than in N2 or N9, in contrast to N1 (**Table 2**). The N7 nanocomposite contains more iron than copper (Fe/Cu ~ 20), which is bound to sulfur (S/Fe ~ 0.1) and oxygen (O/Fe ~ 2), implying the presence of FeS (*i.e.* $Fe^{2+}S^{2-}$) and FeOOH compounds. We suggest that N7 may also contain $Cu^+Fe^{3+}S_2$ and $Cu^+Fe^{2+}Fe^{3+}S_3$ because S/Cu ~ 2.6 (**Table 2**). We assume the presence of Cu-CO(O) and CuO in N7 (O/Cu ~ 46 and C/Cu ~ 13). For comparison, N2 can contain CuS (S/Cu ~ 1) and CuO (O/Cu ~ 8). The carbon lattice is intercalated with a greater amount of sulfur in N2 than in N9 (C/S ~ 16 and ~ 72).

Table 2. The values of atomic concentration (atom.%) estimated from peak areas corrected by the sensitivity factor (SF) for the chemical bonds derived from the XPS spectral lines of synthesized GO (sample N1), copper@GO (sample N2), copper/iron@GO (sample N7) and iron@GO (sample N9).

Atom.%	C	O	S	Fe	Cu	Na	Ca	Cl
N1	62.8	36.7	0.6	-	-	-	-	-
N2	61.3	29.2	3.8	-	3.8	1.4	0.6	-
N7	15.7	55.2	3.1	24.2	1.2	-	-	0.7
N9	65.2	27.1	0.9	4.9	-	1.6	0.3	-

We ascertain that in N9 iron hydroxides and oxides such as $Fe^{3+}O^{2-}(OH)^-$, $Fe^{2+}(OH)_2^-$, $Fe^{3+}(OH)_3^-$, Fe_2O_3 and $Fe^{2+}O^{2-}$ may be also present. In N2 and N9 XPS spectra confess the appearance of Na KLL Auger lines at 534-541 eV that overlap with O1s, suggesting the presence of NaOH and Na_2SO_4. In N9 FeS with Fe^{2+} and S^{2-} oxidation states and SO_4 can be formed. We expect that the presence of negligible amount of sodium compounds in both N2 and N9 may be also contributed by the acoustic cavitation impact on the glass walls of a reaction vessel due to diffusion processes,[100,101] in addition to the sonochemical reactions involving Na_2S and radical species.

The XPS Cu2p lines reveal main component peaks for the Cu^+ (designated as Cu (I)) in N2 and N7, proving the formation of Cu^+S^-, $Cu_2^+S^{2-}$ and $Cu_2^+O^{2-}$ (**Figure S2A**). The existence of

FULL PAPER Accepted Article

the Cu^{+} state in N2 and N7 was also confirmed by the Cu LMM Auger line at ~ 918 eV (**Figure S2B**). We do not exclude the possible formation of metallic copper because its binding energy value is at ~ 933 eV and ~ 952.75 eV.[102] We suggest that no $CuCO_3$ or $Cu(OH)_2$ are produced because their binding energies for the $Cu2p_{3/2}$ and $Cu2p_{1/2}$ lie at higher values, *i.e.* 935 eV and 955 eV for the first compound, and 937 eV and 957 eV for the second compound. To note, the appearance of $CuCO_3$ is associated with the C1s peak at 287.5 eV and O1s at 533.9 eV, which are not observed in either N2 or N7. In addition, we exclude the formation of $CuSO_4$ and $Cu_3(SO_4)(OH)_4$ because the XPS Cu2p also have higher binding energy values (935.2 eV and 955.0 eV).[99] To note, small broad peak at 934.8 eV and shake-up components at 943.5 eV and 963.8 eV appear only in N2, disclosing the Cu^{2+} state,[99,102,103] which can be attributed to the formation of $Cu^{2+}S^2$ and $Cu^{2+}O^{2-}$.[104-107] High temperature (~ 800°C) may lead to the appearance of Cu_2O preventing CuO formation.[108] On the other hand, the reduction of CuO to Cu_2O may be expected from the decomposition to Cu_2O at > 1073°C.[109] Such high temperature can be created by hot spots during acoustic cavitation.[110]

The XPS Fe2p line reveals a doublet at ~ 711.6 eV and ~ 725.6 eV in both N7 and N9, denoting hydrated iron oxide[111] or ferric oxidation products **(Figure S2C)**.[112] This doublet may be indicative for $Fe^{2+}O^{2-}$, hematite α-Fe_2O_3 (~ 711.4 eV), γ-Fe_2O_3 (~ 711.8 eV), hydroxyl-oxide FeO(OH) that may have an intermediate composition between goethite α-FeOOH (711.8 eV) and α-Fe_2O_3.[113] Small satellite peaks (at ~ 719.8 eV and ~ 733.2 eV) appear only in N7, designating for Fe^{3+} in FeO(OH) and Fe_2O_3. It is important to note, that magnetite (*i.e.* Fe_3O_4) compound is not detected on the surface of neither N7 nor N9, in agreement with the XRD bulk material analysis (**Figure 2**). Usually the formation of magnetite requires low temperature (< 100°C) and reducing conditions, meaning low or no-oxygen environment. The presence of the sulfate ion may lead first to the formation of iron oxyhydroxysalts followed by transformation into goethite,[114] which is a product of pyrite oxidation.[115] Pyrite oxidizes to produce S and SO_4, and the formation of S is restricted to the order of a monolayer in basic aqueous solution. Products of pyrite dissolution in alkaline medium are hematite α-Fe_2O_3 and ferrihydrite. We suggest that hematite is present in both N7 and N9, whilst ferrihydrite can be produced only in N9 because of the higher O/Fe ratio (~ 6 in N9 and ~ 2 in N7). Reduction of iron hydroxide in the presence of S leads to the formation of iron sulfide. We assume that iron hydroxide can be formed on the pyrite surface in N9 because of stronger OH peak relatively to O in **Figure 3B**.

We suggest that SO_4 ions are adsorbed by Fe_2O_3 via the replacement of two OH groups by forming a bridge bond Fe-O-S.[116] The formation of $FeCO_3$ and $Fe(OH)_2CO_3$ may be excluded because of the lower binding energy values, *i.e.* ~ 710.2 eV ($Fe2p_{3/2}$) and ~ 723.7 eV ($Fe2p_{1/2}$). We also may exclude the presence of metallic iron because its binding energy value lies at ~ 706.7 eV ($Fe2p_{3/2}$) and ~ 720.3 eV ($Fe2p_{1/2}$). The presence of FeS and $FeSO_4$ (also $Fe_2(SO_4)_3$) on the surface of N7 is less probable (~ 712.2 eV and ~ 712.1 eV), but not in N9, where there may be a small contribution of both these substances as a result of a broadened peak at 711.6 eV. To note, the XRD analysis of N9 bulk material reveals the FeS phase (**Figure 2**), pointing out that iron sulfate may be exclusively located on the surface. The reason why FeS is not detected either in the bulk or on the surface of N7 may be

explained by the reaction of iron with copper resulting in binary $Cu^+Fe^{3+}S_2$ and $Cu^+Fe^{2+}Fe^{3+}S_3$ compounds. The presence of sulfates is confirmed by the appearance of a relatively broad XPS S2p doublet at 168-171 eV in N1 and each nanocomposite (**Figure S3**).[96,99] In N7 the XPS line at ~ 162-164 eV is broad and small, and may be attributed to the doublet for the Cu^+S^- (162.0 eV), $Cu_2^+S^{2-}$ (162.4 eV) and $Fe^{2+}S_2^-$ (162.9 eV). In N2 $Cu_2^+S^{2-}$ (161.2 eV) and $Cu^{2+}S^{2-}$ (162.06 eV) can be present, while in N9 a broad peak may be attributed to $Fe^{2+}S_2^-$ (162.9 eV).

Sonochemical formation mechanism of copper/iron-modified@GO nanocomposites

Let us refer to the sonochemical synthesis in order to understand the formation mechanism of prepared nanocomposites. This sonochemical synthesis is conducted in three successive steps: 1) ultrasonic treatment of the synthesized GO with Na_2S acting as a strong reductant; 2) sonication of previously treated GO in aqueous solution containing Cu^{2+} and Fe^{3+} ion precursors; 3) ultrasonic treatment of the sonochemically preformed copper or iron - modified GO with Na_2S.

In the first step water undergoes sonolysis, producing hydrogen and hydroxyl free radicals (H· and OH·) and their recombination products such as molecular hydrogen (H_2) and hydrogen peroxide (H_2O_2).[77] In an oxygenated aqueous solution, additional hydrogen peroxide may be formed by a route involving hydroperoxyl (HO_2) radical. We assume that these radical species are not scavenged as no additives were added during the synthesis. Treatment of GO with Na_2S leads to the reduction of GO and intercalation of S ions into the carbon lattice,[85] yielding S-rGO with a C-S bond acting as a mild oxidizer. We assume that S is most probably intercalated in the carbon lattice of GO by substitution with oxygen and this reaction is enhanced by acoustic cavitation (jets, shock waves, capillary waves).[100] Oxidation of unreacted S forms SO_3 followed by SO_4 through the nucleophilic reaction between the surface OH and epoxy groups of GO.

In the second step Cu^{2+} and Fe^{3+} will react with the S-rGO, sulfate ions (adsorbed on GO) and sonochemically formed radical species. Metal ions will react with sonochemically produced H· (reductant) and a number of oxidizers such as OH·, H_2O_2 and $O_2·$ and lead to the oxidation of copper and iron in the form of sulfides or oxides (hydroxides). According to the oxidation potentials of Cu and Fe,[104] Cu^{2+} will remain in its oxidation state as Cu^+ is not stable in the presence of Fe^{3+}. According to the standard chemical potentials of Cu and Fe,[105] Cu^{2+} and Fe^{3+} will react with S and undergo oxidation, yielding copper and iron oxides/sulfides and iron hydroxides. The structure of CuS can be introduced by trigonal Cu ion bridge Cu_3S-CuS_3 with the disulfide layer (S-S).[85] Oxidation of CuS produces sulfates. Pyrite oxidation in alkaline medium (our solutions have pH = 10) causes reduction of Fe^{2+} and formation of SO_4.[111] Product of pyrite oxidation is Fe^{3+} oxyhydroxide, *i.e.* goethite α-FeOOH.[115] In addition, ultrasound also causes dissolution and hydrolysis of chemical substances,[117] whilst oxidation and dissolution reactions are not well-distinguished processes.

In the third step sonochemical reactions proceed with the excess amount of a strong reductant (Na_2S/Me molar ratio is ~ 100) meaning that the dominant reaction will be reduction. Faster and easier reduction will proceed at higher values of the standard chemical potential of metals, *i.e.* the reduction from

FULL PAPER Accepted Article

ferric Fe^{3+} to ferrous Fe^{2+} will be faster and more favorable than from Cu^{2+} to Cu^+, while formation of metallic compounds (*i.e.* Fe^0 and Cu^0) will proceed very slowly. Sonochemical reduction may also lead to the formation of binary compounds such as $Cu^+Fe^{3+}S_2$ (chalcopyrite) and $Cu^+Fe^{2+}Fe^{3+}S_3$ (cubanite), taking into account similar system with Ag.[117] Strong reducing conditions will lead to the formation of iron hydroxide, which may have an intermediate composition between α-FeOOH and α-Fe_2O_3 (at pH = 10). Outer hydrous FeOOH may act as a matrix for the Fe^{3+}/Fe^{2+} reactions. In this case possible reaction products could be Fe_2O_3, $Fe(OH)_2$, Cu_2S and Cu_2O.

Sonochemical intercalation of ketorolac into copper/iron-modified@GO nanocomposites

We used the anti-inflammatory drug ketorolac in its pristine powder form for the sonochemical intercalation into GO nanocomposites with the aim to prepare effective nanoscale carrier (**Figure S4**). The molecular drug intercalation into GO nanocomposites was examined by Raman microscopy (**Figure 4**).

Raman spectra reveal characteristic bands of ketorolac being in agreement with many NSAIDs[118] and D (1360 cm^{-1}) and G (1606 cm^{-1}) main peaks of GO[119] (**Figure 4A**). Most of these Raman peaks from the ketorolac appear in the synthesized GO (N1), copper@GO (N2) and copper/iron@GO (N7) nanocomposites, but are broader and less defined in iron@GO (N9) nanocomposite (**Figure 4B** and **C**).
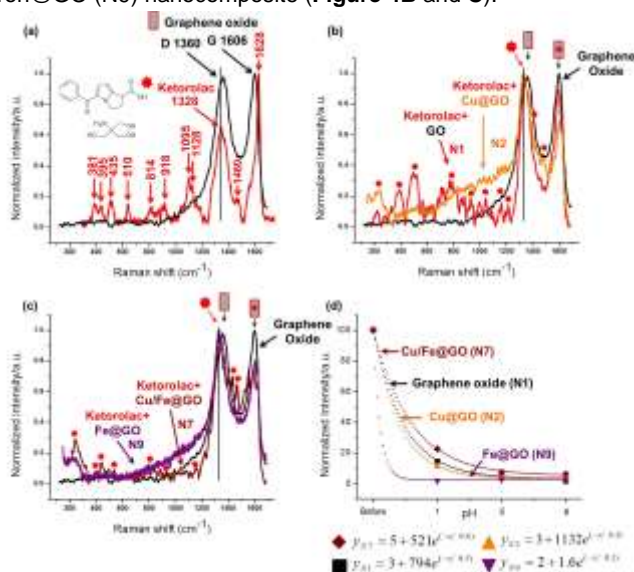

Figure 4. (a) Averaged Raman spectra of synthesized GO (black line) and bulk microscopic ketorolac powder (Ketorolac, red line); (b) ketorolac being intercalated into the synthesized GO (sample N1, red line) and copper@GO (sample N2, orange line) nanocomposites; (c) ketorolac being intercalated into the copper/iron@GO (sample N7, wine line) and iron@GO (sample N9, violet line) nanocomposites. At least five Raman spectra were collected with 10 s of integration time for an individual spectrum acquisition at 6x10^{-3} W laser power and 633 nm excitation wavelength. (d) Plot of normalized intensity of prominent Raman peak of ketorolac (~ 1328 cm^{-1}) before and after incubation of the drug loaded GO nanocomposites in aqueous solution adjusted to one of the following pH values: 1, 5 and 8. Experimental data (dots of different shapes and color coding) are fitted with the exponential decay curves according to the mathematical equations y_{N1}, y_{N2}, y_{N7} and y_{N9} with the calculated decay constants: 0.6 (sample N7), 0.5 (sample N1), 0.4 (sample N2) and 0.1 (sample N9).

Importantly, the prominent Raman peaks from the ketorolac at 1328 cm^{-1} and 1628 cm^{-1} appear as strong bands in all

nanocomposites (**Figure 4**). In each GO nanocomposite the intense Raman peak of ketorolac at 1328 cm^{-1} originates from a characteristic band of the γ-amorphous form of ketorolac.[118] This prominent Raman peak of ketorolac develops a small shoulder closer to the D band of GO, and its stronger delocalization illustrates the significant contribution by carboxylate groups. This amorphous form of ketorolac may contain a range of molecular conformations and intermolecular bonding arrangements. Another prominent Raman peak of ketorolac at 1628 cm^{-1} is shifted towards the G band of the GO in N1 and N9, but not in N2 and N7, and appears as a shoulder in all samples, perturbing the G peak, indicating particular binding or complexation mechanisms,[119] which we cannot distinguish at the moment (**Figure S5**).

Next, we were interested in understanding why explicit Raman peaks of ketorolac appear as multiple bands in copper/iron@GO than in copper@GO or iron@GO nanocomposites. Heretofore the functioning mechanism of ketorolac (like many other NSAIDs) is not completely understood, but may be related to prostaglandin synthesis inhibition.[120] It is accepted that the biological activity of ketorolac tromethamine is associated with the S-form having analgesic activity. We found a model dye, S-containing methylene blue (MB) that is Raman active and has a similar chemical structure to the ketorolac that can be used for the sonochemical intercalation into GO nanocomposites to reveal the binding mechanism of this drug under acoustic field. In contrast to ketorolac, Raman spectra show multiple characteristic peaks of MB after sonochemical intercalation into copper@GO, copper/iron@GO and iron@GO nanocomposites (**Figure S6**). In these spectra strong Raman bands of MB appear at 1326 cm^{-1} and 1396 cm^{-1} being assigned to $_α$(C-H) in-plane ring deformation, at 1431 cm^{-1} and 1441 cm^{-1} designating $_{vasym}$(C-N) and at 1624 cm^{-1} demonstrating $_v$(C-C) ring vibration. These Raman bands develop shoulders at 1360 cm^{-1} and 1606 cm^{-1} corresponding to the characteristic Raman D and G bands of GO, evidencing successful intercalation of MB into all three types of nanocomposites.

Intense peak at 447 cm^{-1} is attributed to the $_δ$(C-N-C) skeletal bending band of MB, indicating that the molecules were adsorbed on the surface of GO nanocomposites.[121] The shifted small Raman peak (600 cm^{-1}) designates $_δ$(C-S-C) vibration, suggesting that sonochemical intercalation of MB into nanocomposites may access via the linkage with S and the carbon lattice or via the complexation with CuS or FeS sites including interaction with the sulfate groups. Negligible Raman peaks positioned at 677 cm^{-1} and 1039 cm^{-1} may signify the out-of-plane bending $_γ$(C-H) and $_β$(C-H), and at 1183 cm^{-1} may specify the stretching $_v$(C-N) bond of MB, suggesting the in-plane intercalation of MB into the GO carbon network structure.

Ketorolac disintegration test in aqueous solutions adjusted to pH values from 1 to 8

For drug delivery application, we examined the drug disintegration from the sonochemically prepared GO nanocomposite carriers through the detection of a prominent Raman peak of ketorolac (1328 cm^{-1}) before and after incubation in aqueous solutions adjusted to the following pH values 1, 5 and 8 (**Figure 4D**). These pH values were chosen in accordance with the pH values of human gastric juice in stomach (~ 1.5-3.7),[76] lysosomes (~ 4.3-5.3),[77] urine (~ 5.9-6.7),[78] duodenum (~ 6.0-8.0),[79] and pancreas or insulin secretion (~ 5.0-10.5).[80] Disintegration of ketorolac from the GO nanocomposites was

compared to the pristine GO with the aim to find out the usefulness of copper, copper/iron or iron compounds in the binding to ketorolac. Overall the Raman intensity of ketorolac in each GO material monotonically decreases following the exponential decay curve if the pH of aqueous solutions was increased from 1 to 8. From the values of the peak intensity at maximum conditions of the precipitant (**Figure 4D**), one can estimate the peak intensity decay values from the drops of supernatant at the studied pH values in terms of the approximate amount of the unreacted ketorolac (in mg) after the incubation (**Table S2**).

However, the rate of Raman intensity decay of ketorolac depends on the type of GO nanocomposite over the selected pH range. In particular, the decay constant of copper/iron@GO nanocomposite is much larger (~ 0.6) than of iron@GO material (~ 0.1), suggesting the faster disintegration of ketorolac in iron@GO amongst all types of GO nanocarriers starting from low pH values. In contrast, ketorolac is still entrapped in copper/iron@GO carrier at acidic conditions and slowly disintegrates at pH values increased to 8. The disintegration of ketorolac from pristine GO and copper@GO is comparable with a decay constant being 0.5 and 0.4, suggesting that the complexation of ketorolac with copper in the carbon structure of GO enriched with oxygen compounds is important for drug retaining. This action is strengthened by the presence of both copper and iron compounds in sonochemically modified GO (sample N7). In addition, at pH = 5 and 8 the surface of GO is enriched with COO⁻ groups and GO becomes more hydrophilic, while the drug is hydrophobic, meaning that the trapped ketorolac in the GO will stay in the fluid flow for extended period of time. This finding suggests that ketorolac intercalated into the copper/iron@GO nanocomposite may survive aggressive gastric medium avoiding harmful action on stomach cells and most probably stay in the flow of aqueous medium for the targeted delivery.

Conclusions

Two feasible sonochemical methods for the formation of novel graphene oxide-based nanocomposites and for the intercalation of the nonsteroidal anti-inflammatory drug ketorolac have been demonstrated here. First, an accessible sonochemical method for the modification of graphene oxide with copper, copper/iron and iron compounds from graphite has been developed using aqueous solution of copper and iron ion precursors and ultrasound (20 kHz, 18 W/cm²). Unique copper@GO, copper/iron@GO and iron@GO nanocomposites acquire a reduced size (< submicron) than pristine GO and a higher surface area enriched with Cu_2O, CuO, Fe_2O_3, $FeO(OH)$ and sulfur- or carbon-containing compounds. These nanocomposites have been examined as potential nanoscale carriers for ketorolac entrapment and disintegration in aqueous solution. Second, a convenient single-step sonochemical method for the intercalation of ketorolac has been developed using ultrasound (20 kHz, 8 W/cm²) for 3 min under ambient conditions. Ketorolac monotonically disintegrates at a slower rate from copper/iron@GO amongst all other nanocomposites after incubation in aqueous solution adjusted to a pH from 1 to 8 due to the more efficient complexation with GO in the presence of both copper and iron compounds in the carbon lattice

structure. Iron@GO has been revealed as the least efficient nanocarriers because of the faster ketorolac disintegration at acidic conditions. In contrast, ketorolac is still entrapped in the copper/iron@GO nanocomposite at low pH and slowly disintegrates at increased pH values, meaning that this drug may potentially stay in the flow of aqueous medium for extended period of time, important for targeted delivery. We believe that the developed sonochemical method has a potential to be successfully applied to other NSAIDs.

Experimental Section

Materials

Graphite was purchased from IMERYS, France (detailed information about the graphite size and elemental composition can be found in supporting information). $Na_2S \cdot 9 \cdot H_2O$, $CuCl_2 \cdot 2 \cdot H_2O$, isopropanol, H_3PO_4, $KMnO_4$, H_2SO_4, H_2O_2 (60%), HCl (35%), HNO_3 (40%), C_2H_5OH, $FeCl_3$ 6 H_2O, methylene blue are of higher grade purity 99% being obtained from Belreachim JSC (Belarus). Silver nitrate ($AgNO_3$, analytical grade, 99.8 %) and sodium borohydride ($NaBH_4$, 98 %) were obtained from Sigma-Aldrich Co. (Germany). Distilled water (pH = 5.5, specific conductivity 5 µS/cm) was prepared by using a homemade distillation apparatus (Belarus). We synthesized graphene oxide (GO) using the improved Hummers method[122] (more details in supporting information). Ketorolac was purchased from Dr. Reddy's Inc. (India). For experiments 10 tablets of ketorolac were grinded in a mortar until a fine powder was obtained (more details in supporting information). This powder was dissolved in 3 mL of ethanol at a critical concentration of dissolution being 7 g/L. Methylene blue solutions were prepared at a concentration 1x10⁻⁶ mol/L in DI water and filtered through a cellulose membrane filter (red line, the pore size 8-12 nm).

Sonochemical synthesis of copper/iron@graphene oxide nanocomposites

In all our sonochemical experiments we used a homemade horn-type ultrasonic disperser N.4-20 operating in a continuous mode at 20 kHz frequency with the 400 W maximal output power. This ultrasonic disperser was specifically designed by Cavitation Inc. (Belarus) for the preparation of emulsions and colloidal suspensions. The ultrasonic intensity of this ultrasonic device was calibrated by using a method of calorimetry.[123]

Powder of synthesized GO was dispersed in DI water (pH = 5.5) by sonication (18 W/cm² for 30 min) at a volume ratio of powder suspension (0.6 g/L) to water as 1:1 under ambient air in the ice bath. As the next step 5 mL of 1 M Na_2S aqueous solution was added into the sonicated GO suspension. The colloidal solution of {Na_2S and GO} was sonicated in a sealed thermostatic round-bottomed cylindrical container (T = 60°C) for 1 h at 8 W/cm² ultrasonic intensity. When sonication was finished, this mixture was cooled down to room temperature and the powder was precipitated by centrifugation at 4.293,12 x g for 30 min. The supernatant was removed and the precipitant was added by 5 mL of aqueous solution of 10 mM $CuCl_2$ and 5 mL of aqueous solution of 10 mM $FeCl_3$ and this mixture was sonicated at 18 W/cm² for 2 h in a sealed thermostatic container in the ice bath. Then 5 mL of 1 M Na_2S aqueous solution was added into the sonicated mixture and ultrasonically treated (18 W/cm² for 1 h) in the ice bath. After that the colloidal dispersion (pH = 12) was centrifuged at 4.293,12 x g for 30 min

FULL PAPER Accepted Article

and the supernatant was carefully removed. The precipitant was dispersed in DI water (pH = 5.5) and washed by centrifugation three times until the final pH value of the colloidal dispersion reached 5.5. This suspension was dried in the oven at 100°C and the fine black powder was obtained.

In addition, we also performed the synthesis of nanocomposites without $CuCl_2$ by taking 10 mL of aqueous solution of 10 mM $FeCl_3$, and without $FeCl_3$ at different concentration of aqueous solution of $CuCl_2$ (5 mM, 10 mM and 25 mM) at 0.5 M or 1 M Na_2S at a constant volume ratio of $Na_2S:CuCl_2$ as 1:2. These nanocomposites were designated as copper-modified@GO (without Fe) and iron-modified@GO (without Cu). All sonochemically prepared surface modified GO nanocomposites are designated as follows: a) **N1**: synthesized GO; b) **N2**: copper-modified@GO; c) **N7**: copper/iron-modified@GO and d) **N9**: iron-modified@GO.

Intercalation of ketorolac into copper, copper/iron- and iron@GO nanocomposites

3 mg of copper/iron-modified@GO nanocomposites were added by 3 mL of freshly prepared solution of ketorolac (at 7 g/L of a critical concentration of dissolution in ethanol) and sonicated in 3 mL of DI water (pH = 5.5) at 8 W/cm² for 3 min. Then the mixture was centrifuged at 4.293,12 x g for 15 min in order to remove the unreacted chemical residuals. For Raman measurements the ketorolac loaded GO nanocomposites were modified with silver as the following. After centrifugation cycles the precipitant was added by 3 mL of freshly prepared ice-cold aqueous solution of 7 mM $NaBH_4$ and the colloidal suspension was sonicated in the ice bath. During first minutes of sonication 1 mL of fresh 1 mM $AgNO_3$ aqueous solution was dropwise added into this colloidal dispersion and ultrasonic treatment was immediately stopped. This dispersion was added by 3 mL of ketorolac solution followed by 3 min of sonication, removed from the ultrasonic reaction vessel and left for one hour at room temperature in a dark place. For comparison, we performed ultrasonic treatment of colloidal GO dispersions (*i.e.* N1, N2; N7 and N9) containing methylene blue dye instead of ketorolac (more details in supporting information).

Drug disintegration test

1 mL of each colloidal suspension containing surface modified GO nanocomposites loaded with ketorolac were incubated in 1 mL of DI water adjusted to one of the following pH values: 1, 5 and 8. Samples were withdrawn after 7 h, washed by repeated centrifugation at 4.293,12 x g for 30 min in order to remove the unreacted chemical residuals and diluted with DI water. Drops of these aqueous dispersions were placed on glass or Al_2O_3 substrates and left for 8 h of drying at room temperature. The presence of intercalated ketorolac was examined by its prominent characteristic peak at 1328 cm⁻¹ by using Raman microscopy.

Characterization

The synthesized nanocomposites were characterized through several methods: Dynamic Light scattering (DLS), Zeta Potential (ZP), scanning electron microscopy (SEM) and energy dispersive X-ray fluorescence (EDX), X-ray powder diffraction (XRD), X-ray photoelectron spectroscopy (XPS) and confocal Raman microscopy. The size distribution and ξ-potential of nanocomposites were measured by DLS from Malvern Instruments Ltd. by using a Zetasizer Nano instrument and a buffer solution of DI water (pH = 5.5). DLS and ξ-potential (electrical charge) experiments were carried out on a 50 times diluted colloidal suspension. Each measurement took 10 s; the

nanoparticle distribution and electrophoretic curves were obtained by averaging ten measurements.

The morphology and elemental composition of sonochemically prepared nanocomposites were analyzed and characterized by SEM (S-4800) Hitachi, Japan. The phase composition was characterized by using powder diffraction patterns recorded with an EMPYREAN diffractometer (PANalytical, Netherlands) using Cu-Kα radiation (Ni-filter) at 296 K. X-ray photoelectron spectra (XPS) of our nanocomposites were measured by using a custom XPS spectrometer equipped with hemispherical electron energy analyzer and monochromatized X-Ray $Al_{Kα}$ source with hv = 1486.6 eV and a spot size of 0.3 mm (SPECS GmBH, Germany) in ultra-high vacuum (UHV) conditions. Original XPS spectra were corrected for a Shirley background and fitted by Gaussian-Lorentzian peak shape (red line) by using the KolXPD 1.8.0 software developed by scientists in the Charles University of Prague, Faculty of Mathematics and Physics/Surface Physics (https://www.kolibrik.net/kolxpd).

Raman spectra were recorded by using a 3D inverted confocal Raman microscope Confotec NR500 from SOL Instruments Ltd. (Belarusian-Japanese joint venture "SOLAR TII") at 633 nm excitation wavelength with a grating 600gr/mm blazed at 600 nm. The dried powder, which was modified with silver, was placed on a cover slip for laser excitation under ambient air. The Si wafer with the characteristic Raman line at 520 cm⁻¹ was taken as a reference for calibration and basic alignment during integration time from 0.3 to 1 s. The acquired Raman and SERS spectra were corrected for the baseline and a background of the Si wafer. A linearly polarized diode laser beam was focused through the objectives with the 100x magnification for Raman spectra acquisition. The laser power was attenuated by using neutral density filters, which allow the transmission of a laser beam with respect to the optical density of the filter according to the equation $OD=-log(T)$ with $T=I/I_0$ (I – transmitted intensity and I_0 – incident laser intensity). The following values of OD (T) were used 0.6 (25), 0.3 (50) and no filter (100).

Acknowledgements

FULL PAPER Accepted Article

[1] K. H. Maniar, I. A. Jones, C. T. Vangsness, R. Gopalakrishna, *Expert Opin. Pharmacother.* **2018**, *19*, 93-102.

[2] P. Marzuillo, L. Calligaris, S. Amoroso, E. Barbi, *Acta Paediatr.* **2018**, *107*, 560-567.

[3] S. K. Samal, S. Routray, G. K. Veeramachaneni, R. Dash, M. Botlagunta, *Sci. Rep.* **2015**, *5*, 9982-9982.

[4] F. J. Flores-Murrieta, V. Granados-Soto, *CNS Drug Rev.* **1996**, *2*, 75-90.

[5] P. Forget, M. Berliere, A. van Maanen, F. P. Duhoux, J. P. Machiels, P. G. Coulie, G. Bouche, M. De Kock, *Med. Hypotheses* **2013**, *81*, 707-712.

[6] G. Sarkar, J. T. Orasugh, N. R. Saha, I. Roy, A. Bhattacharyya, A. K. Chattopadhyay, D. Rana, D. Chattopadhyay, *New J. Chem.* **2017**, *41*, 15312-15319.

[7] E. L. Masso Gonzalez, P. Patrignani, S. Tacconelli, L. A. Garcia Rodriguez, *Arthritis Rheum.* **2010**, *62*, 1592-1601.

[8] S. Wongrakpanich, A. Wongrakpanich, K. Melhado, J. Rangaswami, *Aging and Disease* **2018**, *9*, 143-150.

[9] K. P. Garnock-Jones, *Clin. Drug Investig.* **2012**, *32*, 361-371.

[10] D. Peer, J. M. Karp, S. Hong, O. C. Farokhzad, R. Margalit, R. Langer, *Nat. Nanotechnol.* **2007**, *2*, 751-760.

[11] Y. Min, J. M. Caster, M. J. Eblan, A. Z. Wang, *Chem. Rev.* **2015**, *115*, 11147-11190.

[12] A. E. Nel, L. Madler, D. Velegol, T. Xia, E. M. Hoek, P. Somasundaran, F. Klaessig, V. Castranova, M. Thompson, *Nat. Mater.* **2009**, *8*, 543-557.

[13] W. Gao, J. M. Chan, O. C. Farokhzad, *Mol. Pharmaceut.* **2010**, *7*, 1913-1920.

[14] R. K. Jain, T. Stylianopoulos, *Nat. Rev. Clin. Oncol.* **2010**, *7*, 653-664.

[15] C. M. Dawidczyk, C. Kim, J. H. Park, L. M. Russell, K. H. Lee, M. G. Pomper, P. C. Searson, *J. Control. Release* **2014**, *187*, 133-144.

[16] M. Björnmalm, K. J. Thurecht, M. Michael, A. M. Scott, F. Caruso, *ACS Nano* **2017**, *11*, 9594-9613.

[17] D. Luo, K. A. Carter, D. Miranda, J. F. Lovell, *Adv. Sci.* **2017**, *4*, 1600106.

[18] B. Pelaz, C. Alexiou, R. A. Alvarez-Puebla, F. Alves, A. M. Andrews, et.al., *ACS Nano* **2017**, *11*, 2313−2381.

[19] X. Wang, T. Xia, M. C. Duch, Z. X. Ji, H. Y. Zhang, R. B. Li, B. B. Sun, S. J. Lin, H. Meng, Y. P. Liao, M. Y. Wang,T. B. Song, Y. Yang, M. C. Hersam, A. E. Nel, *Nano Lett.* **2012**, *12*, 3050−3061.

[20] X. Wang, M. C. Duch, N. Mansukhani, Z. X. Ji, Y. P. Liao, M. Y. Wang, H. Y. Zhang, B. B. Sun, C. H. Chang, R. B. Li, S. J. Lin, H. Meng, T. Xia, M. C. Hersam, A. E. Nel, *ACS Nano* **2015**, *9*, 3032−3043.

[21] B. Fadeel, C. Bussy, S. Merino, E. Vázquez, E. Flahaut, et.al. *ACS Nano* **2018**, *12*, 10582−10620.

[22] R. Cini, *Comments Inorg. Chem.* **2000**, *22*, 151-186.

[23] J. E. Weder, C. T. Dillon, T. W. Hambley, B. J. Kennedy, P. A. Lay, J. R. Biffin, H. L. Regtop, N. M. Davies, *Coord.Chem.Rev.* **2002**, *232*, 95 – 126.

[24] N. S. Krstić, R. S. Nikolić, M. N. Stanković, N. G. Nikolić, D. M. Dorđević, *Trop. J. Pharm. Res.* **2015**, *14*, 337-349.

[25] C. N. Banti, S. K. Hadjikakou, *Eur. J. Inorg. Chem.* **2016**, *2016*, 3048-3071.

[26] R. Puranik, S. Bao, A. M. Bonin, R. Kaur, J. E. Weder, L. Casbolt, T. W. Hambley, P. A. Lay, P. J. Barter, K. A. Rye, *Cell Biosci.* **2016**, *6*, 9.

[27] Z. A. Siddiqi, S. Kumar, M. Khalid, M. Shahid, *Spectrochim. Acta Part A* **2009**, *72*, 616–620.

[28] A. Lawal, J. A. Obaleye, *Biokemistri* **2007**, *19*, 9–15.

[29] W. H. Mahmoud, G. G. Mohamed, M. M. I. El-Dessouky, *Spectrochim. Acta Part A* **2014**, *122*, 598–608.

[30] W. Badri, K. Miladi, Q. A. Nazari, H. Greige-Gerges, H. Fessi, A. Elaissari, *Internat. J of Pharmaceut.* **2016**, *515*, 757-773.

[31] A. S. Timin, D. J. Gould, G. B. Sukhorukov, *Expert Opin. Drug Deliv.* **2017**, *14*, 583-587.

[32] S. Senapati, A. K. Mahanta, S. Kumar, P. Maiti, *Signal Transduct. Target Ther.* **2018**, *3*, 7.

[33] C. McCallion, J. Burthem, K. Rees-Unwin, A. Golovanov, A. Pluen, *Eur. J. Pharm. Biopharm.* **2016**, *104*, 235-250.

[34] S. Tran, P. J. DeGiovanni, B. Piel, P. Rai, *Clin. Transl. Med.* **2017**, *6*, 44.

[35] G. Reina, J. M. Gonzalez-Dominguez, A. Criado, E. Vazquez, A. Bianco, M. Prato, *Chem. Soc. Rev.* **2017**, *46*, 4400-4416.

[36] L. L. del Mercato, F. Guerra, G. Lazzari, C. Nobile, C. Bucci, R. Rinaldi, *Nanoscale* **2016**, *8*, 7501-7512.

[37] R. Gui, H. Jin, Z. Wang, F. Zhang, J. Xia, M. Yang, S. Bi, Y. Xia, *Nanoscale* **2015**, *7*, 8289-8293.

[38] M. Rasoulzadeh, H. Namazi, *Carbohydr. Polym.* **2017**, *168*, 320-326.

[39] L. Deng, Q. Li, S. Al-Rehili, H. Omar, A. Almalik, A. Alshamsan, J. Zhang, N. M. Khashab, *ACS Appl. Mater. Interfaces* **2016**, *8*, 6859-6868.

[40] A. Bianco, *Angew. Chem. Int. Ed.* **2013**, *52*, 4986-4997.

[41] L. Ou, B. Song, H. Liang, J. Liu, X. Feng, B. Deng, T. Sun, L. Shao, *Part. Fibre Toxicol.* **2016**, *13*, 57.

[42] A. Sasidharan, L. S. Panchakarla, A. R. Sadanandan, A. Ashokan, P. Chandran, C. M. Girish, D. Menon, S. V. Nair, C. N. Rao, M. Koyakutty, *Small* **2012**, *8*, 1251-1263.

[43] R. Kurapati, J. Russier, M. A. Squillaci, E. Treossi, C. Menard-Moyon, A. E. Del Rio-Castillo, E. Vazquez, P. Samori, V. Palermo, A. Bianco, *Small* **2015**, *11*, 3985-3994.

[44] K. Yang, L. Feng, Z. Liu, *Adv. Drug Deliv. Rev.* **2016**, *105*, 228-241.

[45] K. Haubner, J. Murawski, P. Olk, L. M. Eng, C. Ziegler, B. Adolphi, E. Jaehne, *ChemPhysChem* **2010**, *11*, 2131-2139.

[46] Y. Wang, L. Polavarapu, L. M. Liz-Marzan, *ACS Appl. Mater. Interfaces* **2014**, *6*, 21798-21805.

[47] J. Shi, L. Wang, J. Zhang, R. Ma, J. Gao, Y. Liu, C. Zhang, Z. Zhang, *Biomaterials* **2014**, *35*, 5847-5861.

[48] R. Ortega-Amaya, Y. Matsumoto, A. M. Espinoza-Rivas, M. A. Perez-Guzman, M. Ortega-Lopez, *Beilstein J. Nanotechnol.* **2016**, *7*, 1010-1017.

[49] S. K. Tripathi, R. Goyal, K. C. Gupta, P. Kumar, *Carbon* **2013**, *51*, 224-235.

[50] L. Zhang, Z. Wang, Z. Lu, H. Shen, J. Huang, Q. Zhao, M. Liu, N. He, Z. Zhang, *J Mater. Chem. B* **2013**, *1*, 749-755.

[51] X. Liu, D. Ma, H. Tang, L. Tan, Q. Xie, Y. Zhang, M. Ma, S. Yao, *ACS Appl. Mater. Interfaces* **2014**, *6*, 8173-8183.

[52] B. Karthikeyan, R. Udayabhaskar, S. Hariharan, *Appl. Phys. Lett.* **2016**, *109*, 021904.

[53] R. Cheng, Y. Xue, Carbon Nanomaterials for Biomedical Applications. M. Zhang, R. R. Naik, L. Dai, (Eds.), 2016, XI 576, p. 232 ISBN: 978-3-319-22860-0.

[54] J. Ma, C. Liu, R. Li, J. Wang, *J Appl. Polym. Sci.* **2012**, *123*, 2933-2944.

[55] D. Radziuk, L. Mikhnavets, A. Tkach, L. Tabulina, V. Labunov, *Langmuir* **2018**, *34*, 8599-8610.

[56] S. Kumar, A. Kumar, *Opt. Mater.* **2016**, *62*, 320-327.

[57] S. Sreejith, X. Ma, Y. Zhao, *J. Am. Chem. Soc.* **2012**, *134*, 17346-17349.

[58] D. Jaque, L. Martínez Maestro, B. del Rosal, P. Haro-Gonzalez, A. Benayas, J. L. Plaza, E. Martín Rodríguez, J. García Solé, *Nanoscale* **2014**, *6*, 9494-9530.

[59] S. Srivastava, R. Awasthi, D. Tripathi, M. K. Rai, V. Agarwal, V. Agrawal, N. S. Gajbhiye, R. K. Gupta, *Small* **2012**, *8*, 1099-1109.

[60] X. Shi, H. Gong, Y. Li, C. Wang, L. Cheng, Z. Liu, *Biomaterials* **2013**, *34*, 4786-4793.

[61] Y. Chen, C. Tan, H. Zhang, L. Wang, *Chem. Soc. Rev.* **2015**, *44*, 2681-2701.

[62] U. Shimanovich, A. Gedanken, *J. Mater. Chem. B* **2016**, *4*, 824-833.

[63] R. G. Mendes, A. Bachmatiuk, B. Büchner, G. Cuniberti, M. H. Rümmeli, *J Mater. Chem. B* **2013**, *1*, 401-428.

[64] J. Liu, L. Cui, D. Losic, *Acta Biomater.* **2013**, *9*, 9243-9257.

[65] H. Ali-Boucetta, D. Bitounis, R. Raveendran-Nair, A. Servant, J. Van den Bossche, K. Kostarelos, *Adv Healthc. Mater.* **2013**, *2*, 433-441.

[66] Z. Li, Z. Wang, X. Du, C. Shi, X. Cui, *Adv. Healthc. Mater.* **2018**, *7*, e1701326, 1-22.

[67] K. S. Suslick, *Science* **1990**, *247*, 1439-1445.

[68] K. S. Suslick, D. A. Hammerton, R. E. Cline, *J. Am. Chem. Soc.* **1986**, *108*, 5641-5642.

[69] A. Weissler, *J. Am. Chem. Soc.* **1959**, *81*, 1077-1081.

[70] K. S. Suslick, M. W. Grinstaff, *J. Am. Chem. Soc.* **1990**, *112*, 7807-7809.

[71] B. Lippitt, J. M. McCord, I. Fridovich, *J. Biol. Chem.* **1972**, *247*, 4688-4690.

[72] G. Siljanovska Petreska, M. Salsamendi, A. Arzac, G. P. Leal, N. Alegret, J. Blazevska Gilev, R. Tomovska, *ACS Omega* **2017**, *2*, 4123-4131.

[73] A. Alizadeh, G. Abdi, M. M. Khodaei, M. Ashokkumar, J. Amirian, *RSC Advances* **2017**, *7*, 14876-14887.

[74] K. Vinodgopal, B. Neppolian, I. V. Lightcap, F. Grieser, M. Ashokkumar, P. V. Kamat, *J. Phys. Chem. Lett.* **2010**, *1*, 1987-1993.

[75] B. Neppolian, C. Wang, M. Ashokkumar, *Ultrason. Sonochem.* **2014**, *21*, 1948-1953.

[76] D. E. Beasley, A. M. Koltz, J. E. Lambert, N. Fierer, R. R. Dunn, *PLOS ONE* **2015**, *10*, e0134116, 1-12.

[77] D. E. Johnson, P. Ostrowski, V. Jaumouillé, S. Grinstein, *J. Cell Biol.* **2016**, *212*, 677-692.

[78] A. Kanbara, Y. Miura, H. Hyogo, K. Chayama, I. Seyama, *Nutr J.* **2012**, *11*, 39.

[79] E. M. Quigley, L. A. Turnberg, *Gastroenterology* **1987**, *92*, 1876-1884.

[80] H. H. Sky-Peck, P. Thuvasethakul, *Ann. Clin. Lab. Sci.* **1977**, *7*, 310-317.

[81] D. Radziuk, A. Skirtach, A. Geßner, M. U. Kumke, W. Zhang, H. Möhwald, D. Shchukin, *Langmuir* **2011**, *27*, 14472-14480.

[82] Y. Lee, S. Hanif, P. Theato, R. Zentel, J. Lim, K. Char, *Macromol. Rapid Commun.* **2015**, *36*, 1089-1095.

[83] B. Lavina, P. Dera, E. Kim, Y. Meng, R. T. Downs, P. F. Weck, S. R. Sutton, Y. Zhao, *PNAS* **2011**, *108*, 17281-17285.

[84] C. Zhao, S.-L. Chou, Y. Wang, C. Zhou, H.-K. Liu, S.-X. Dou, *RSC Adv.* **2013**, *3*, 16597-16603.

[85] N. Karikalan, R. Karthik, S. M. Chen, C. Karuppiah, A. Elangovan, *Sci. Rep.* **2017**, *7*, 2494.

[86] A. L assoued, B. Dkhil, A. Gadri, S. Ammar, *Res. Phys.* **2017**, *7*, 3007-3015.

[87] R. V. Kumar, Y. Koltypin, X. N. Xu, Y. Yeshurun, A. Gedanken, I. Felner, *Appl. Phys.* **2001**, *89*, 6324-6328.

[88] L. Machala, J. Tuček, R. Zbořil, *Chem. Mater.* **2011**, *23*, 3255-3272.

[89] M. Gasgnier, L. Beaury, J. Derouet, *Ultrason. Sonochem.* **2000**, *7*, 25-33.

[90] R. Vijayakumar, Y. Koltypin, I. Felner, A. Gedanken, *Mater. Sci. Engineer. A* **2000**, *286*, 101-105.

[91] P. Brázda, J. Kohout, P. Bezdička, T. Kmječ, *Cryst. Growth Des.* **2014**, *14*, 1039-1046.

WILEY-VCH

[92] K. S. Suslick, S.-B. Choe, A. A. Cichowlas, M. W. Grinstaff, *Nature* **1991**, *353*, 414.

[93] B. David, O. Schneeweiss, N. Pizúrová, Šantavá, V. Kudrle, P. Synek, O. Jašek, *Phys. Procedia* **2013**, *44*, 206-212.

[94] D. Yang, A. Velamakanni, G. Bozoklu, S. Park, M. Stoller, R. D. Piner, S. Stankovich, I. Jung, D. A. Field, C. A. Ventrice, R. S. Ruoff, *Carbon* **2009**, *47*, 145-152.

[95] G. Barth, R. Linder, C. Bryson, *Surf. Interface Anal.* **1988**, *11*, 307-311.

[96] Y.-Q. Wang, F.-Q. Zhang, P. M. A. Sherwood, *Chem. Mater.* **1999**, *11*, 2573-2583.

[97] H. Xu, K. S. Suslick, *J. Am. Chem. Soc.* **2011**, *133*, 9148-9151.

[98] D. Gao, G. Yang, J. Li, J. Zhang, J. Zhang, D. Xue, *J. Phys. Chem. C* **2010**, *114*, 18347-18351.

[99] J. F. Moulder, J. Chastain, Handbook of X-ray Photoelectron Spectroscopy. A Reference Book of Standard Spectra for Identification and Interpretation of XPS Data. Ed. by J. Chastain, Perkin-Elmer Corporation, Minesota, USA, **1992,** ISBN: 0-9627026-2-5.

[100] K. S. Suslick, *Faraday Discuss.* **2014**, *170*, 411-422.

[101] M. Virot, T. Chave, S. I. Nikitenko, D. G. Shchukin, T. Zemb, H. Möhwald, *J. Phys. Chem. C* **2010**, *114*, 13083-13091.

[102] D. C. Frost, A. Ishitani, C. A. McDowell, *Mol. Phys.* **1972**, *24*, 861-877.

[103] L. Yin, I. Adler, T. Tsang, L. J. Matienzo, S. O. Grim, *Chem. Phys. Lett.* **1974**, *24*, 81-84.

[104] Ebbing, D.D.; Gammon, S.D. General Chemistry. 9th Edition, Edrs.: Heinle, K.; Galvin, A.; Cava, A. Houghton Mifflin Company, Boston, MA, USA, 2007, ISBN: 0-618-93469-3.

[105] C. M. A. Brett, A. M. O. Brett, Electrochemistry: Principles, Methods, and Applications. Oxford University Press Inc. New York, USA, **1993**, ISBN: 0-19-855388-9.

[106] S. Poulston, P. M. Parlett, P. Stone, M. Bowker, **1996**, *24*, 811-820.

[107] J. P. Tobin, W. Hirschwald, J. Cunningham, *Appl. Surf. Sci.* **1983**, *16*, 441-452.

[108] T. A. Ramanarayanan, J. Alonzo, *Oxid. Met.* **1985**, *24*, 17-27.

[109] A. W. Adamson, Advanced Inorganic Chemistry. By F. A. Cotton and G. Wilkinson. *Inorg. Chem.* **1963**, *2*, 665-665.

[110] Y. T. Didenko, W. B. McNamara, K. S. Suslick, *J. Am. Chem. Soc.* **1999**, *121*, 5817-5818.

[111] A. N. Buckley, R. Woods, *Appl. Surf. Sci.* **1987**, *27*, 437-452.

[112] S. Karthe, R. Szargan, E. Suoninen, *Appl. Surf. Sci.* **1993**, *72*, 157-170.

[113] N. S. McIntyre, D. G. Zetaruk, *Anal. Chem.* **1977**, *49*, 1521-1529.

[114] U. Schwertmann, J. Friedl, H. Stanjek, *J. Colloid Interface Sci.* **1999**, *209*, 215-223.

[115] E. C. Todd, D. Sherman, J. Purton, *Geochim. et Cosmochim. Acta* **2003**, *67*, 881-893.

[116] H. Watanabe, C. D. Gutleben, J. e. Seto, *Solid State Ionics* **1994**, *69*, 29-35.

[117] M. Pilloni, V. B. Kumar, G. Ennas, Z. Porat, A. Scano, V. Cabras, A. Gedanken, *Ultrason. Sonochem.* **2018**, *47*, 108-113.

[118] C. J. Strachan, T. Rades, K. C. Gordon, *J. Pharm. Pharm.* **2007**, *59*, 261-269.

[119] X. Huang, X. Qi, F. Boey, H. Zhang, *Chem. Soc. Rev.* **2012**, *41*, 666-686.

[120] S. Jannath, I. Nayeema, N. Jahan, K. Deepa, *Adv. Bioequiv. Bioavail.* **2018**, *1*, 1-5.

[121] G.-N. Xiao, S.-Q. Man, *Chem. Phys. Lett.* **2007**, *447*, 305-309.

[122] D. C. Marcano, D. V. Kosynkin, J. M. Berlin, A. Sinitskii, Z. Sun, A. Slesarev, L. B. Alemany, W. Lu, J. M. Tour, *ACS Nano* **2010**, *4*, 4806-4814.

[123] M. A. Margulis, I. M. Margulis, *Ultrason. Sonochem.* **2003**, *10*, 343-345.

Supporting Information

Detailed experimental procedures, characterization of synthesized graphene oxide by using DLS, XRD (incl. crystal structure database of X-ray powder diffraction files), TGA and Raman microscopy, and more XPS spectra fitted by using a software KolXPD developed at Charles University (Faculty of Mathematics and Physics/Surface Physics, https://www.kolibrik.net/kolxpd. This material is available free of charge via the Internet at http://pubs.acs.org.

Table of Contents

FULL PAPER (ACCEPTED ARTICLE)

Sonochemically prepared copper/iron@graphene oxide nanocarriers of ketorolac: new feasible sonochemical method is developed for the formation of copper/iron-modified graphene oxide nanocomposites by using ultrasound (20 kHz). These unique nanocomposites are sonochemically intercalated with ketorolac. Ketorolac disintegrates at a slower rate at increased pH (1-8) from these nanocomposites due to the higher surface area enriched with Cu_2O, CuO, Fe_2O_3, $FeO(OH)$ and sulfur- or carbon-containing
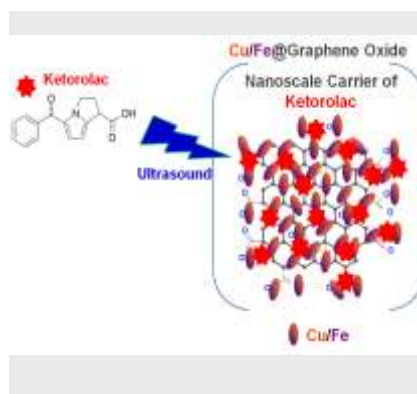
Darya Radziuk,*[a] Lubov Mikhnavets,[a]

Mykhailo Vorokhta,[b] Vladimír Matolín,[b]

Ludmila Tabulina[a], and Vladimir Labunov[a]

Page No. – Page No.

Sonochemical Formation of Copper/Iron-modified Graphene Oxide Nanocomposites for Ketorolac Delivery

[a] Dr. Darya Radziuk,* Lubov Mikhnavets, Dr. Ludmila Tabulina and Prof. Vladimir Labunov
Laboratory of Integrated Micro- and Nanosystems,
Belarusian State University of Informatics and Radioelectronics,
P. Brovki Str. 6, 220013 Minsk, Republic of Belarus
E-mail: dasharaduk@gmail.com
[b] Dr. Mykhailo Vorokhta and Prof. Vladimír Matolín
Department of Surface and Plasma Science,
Charles University of Prague,
V Holešovičkách 2, 18000 Prague 8,
Czech Republic
Supporting information for this article is given via a link at the end of the document.